Training-on-a-Chip: A Multi-Organ Device to Study the Effect of Muscle Exercise on Insulin Secretion in Vitro

Juan M. Fernández-Costa,* María A. Ortega, Júlia Rodríguez-Comas, Gerardo Lopez-Muñoz, Jose Yeste, Lluís Mangas-Florencio, Miriam Fernández-González, Eduard Martin-Lasierra, Ainoa Tejedera-Villafranca, and Javier Ramon-Azcon*

Organ-on-a-chip (OOC) devices bring innovative disease modeling and drug discovery approaches by providing biomimetic models of tissues and organs in vitro combined with biosensors. Miniaturized biosensor systems and tissue biofabrication techniques allow to create multiple tissues on a chip highly controlling the experimental variables for high-content screening applications. In this work, a biomimetic multi-OOC integrated platform composed of skeletal muscle and pancreatic cells is fabricated to study the impact of exercise on insulin secretion. Both engineered tissues are integrated with optical biosensing technology to monitor in real-time the contraction-induced myokine secretion and their effect on beta-cells insulin production. Using this device, it is demonstrated that insulin secretion is induced directly by the effect of myotubes contractions. The cross-talk platform would improve drug assays and provide a new model to study the loss of pancreas functionality associated with diabetes mellitus.

1. Introduction

The pharmaceutical industry depends on in vivo animal models and in vitro standard 2D cell cultures for drug development.

J. M. Fernández-Costa, Ma. A. Ortega,[+] J. Rodríguez-Comas,[++]
G. Lopez-Muñoz, J. Yeste,[+++] L. Mangas-Florencio, M. Fernández-González, E. Martin-Lasierra, A. Tejedera-Villafranca, J. Ramon-Azcon
Institute for Bioengineering of Catalonia (IBEC)
The Barcelona Institute of Science and Technology (BIST)
C/Baldiri Reixac 10–12, Barcelona E08028, Spain
E-mail: jfernandez@ibecbarcelona.eu; jramon@ibecbarcelona.eu
J. Ramon-Azcon
Institució Catalana de Recerca i Estudis Avançats (ICREA)
Passeig de Lluís Companys, 23, Barcelona E08010, Spain

The ORCID identification number(s) for the author(s) of this article can be found under https://doi.org/10.1002/admt.202200873.

[+]Present address: Vitala Technologies S.L., C/de Gironella, 49, E08017 Barcelona, Spain
[++]Present address: Sycai Technologies S.L., C/de Roc Boronat, 117, MediaTIC Building, E08018 Barcelona, Spain
[+++]Present address: Brigham and Women's Hospital, Harvard Medical School, 77 Avenue Louis Pasteur, Boston, MA 02115, USA

The limitations associated with the current in vivo and in vitro models are exemplified by the significant number of new drug candidates that fail to reach the market due to low efficiency or severe side effects in humans. These shortcomings, together with regulatory restrictions limiting the use of animal models, have generated interest in developing human-based tissue-like constructs coupled with biosensor technologies (e.g., organs-on-a-chip, OOC) for disease modeling and drug and chemical testing.[1–3] To date, most of the OOC devices available represent a single organ, preventing investigations on systemic drug effects. Therefore, the current challenges of these microscale tissue analog systems attempt to improve the prediction of the effects of drugs and toxicity on various organs or tissues. This is especially important for studying multisystemic diseases when several tissues are closely related to the disease, as are skeletal muscle and pancreatic islets for diabetes mellitus (DM). In the present day, there are few examples of multi-organ devices representing various organs or tissues. We can find examples of multiple cell types (liver, tumor, and bone marrow or lung, kidney, and adipose cells) cultured in separate chambers interconnected and used to test the toxicity of drugs.[4,5] Or co-cultures for intestine, liver, and breast cancer cells to evaluate the intestinal absorption, hepatic metabolism, and drugs' anti-target cell bioactivity.[5] Notwithstanding the continued efforts and strong motivations to replace animal testing, these multi-organ systems are still in their infancy. Fully functional tissues have been recently incorporated into a multi-organ approach.[6] This device linked heart, liver, bone, and skin tissues by recirculating vascular flow to study pharmacokinetics and pharmacodynamic profiles. However, this device did not incorporate sensing technologies to monitor the metabolic dynamics of the tissues in real-time.

DM comprises a group of chronic metabolic diseases characterized by hyperglycemia. DM is a major public health problem worldwide since the number of patients suffering increases every year.[7] Type 2 diabetes (T2D), the most common form of this disease, accounts for 90–95% of cases of DM.[8] T2D typically arises when peripheral metabolic tissues no longer respond to the insulin action to lower glucose levels in the blood. Skeletal muscle is one of the primary tissues targeted by insulin and is also involved in the glucose homeostasis

**ADVANCED
SCIENCE NEWS**
www.advancedsciencenews.com

**ADVANCED
MATERIALS
TECHNOLOGIES**
www.advmattechnol.de

maintenance. Therefore, defects in glucose uptake by skeletal muscle contribute to insulin resistance in T2D.[9,10] Mainly, myokines released by muscle cells (such as interleukin 6) impact the self-regulation of skeletal muscle glucose metabolism. The pancreas has a critical role in T2D. The endocrine function of the pancreas comprises approximately a million cell clusters called islets of Langerhans.[11] In pancreatic islets, beta-cells produce, store and release insulin. The progressive beta-cell failure and the loss of beta-cell mass in the pancreas are the other key factors in T2D.[12]

Various approaches have been used to study the fundamental biology of muscle tissues, the molecular pathways of diseases related to them, and their regenerative capability.[13–15] Future challenges to on-chip skeletal muscle models include robust approaches to monitoring glucose uptake and other events in real-time (e.g., secretion of myokines and contraction dynamics), co-culture with other cells and tissues, and long-term maintenance of functional muscle myofibers. Recent findings in pancreatic engineered tissues point toward 3D culture systems as promising platforms to improve the clinical outcome of islet transplantations.[16,17] While the 3D microorganization of cells is key to engineering these tissues with similar functionality as in vivo, no 3D approaches have been described for in vitro drug discovery and T2D metabolic studies.

OOC devices accurately represent in vivo organ physiology and drug pharmacokinetics through precise control of cellular microenvironments.[6,1] In addition, monitoring tissue physiology by quantitative data acquisition is also essential. Future OOC devices should allow high-throughput analyses where tissues in 3D are integrated with a sensor platform capable of collecting relevant data in a short time. Current OOC assays rely heavily on fluorescence techniques and have mainly been used for specialized proof-of-concept studies to study angiogenesis,[9,18,19] electrophysiology,[20,21] and pharmacological modulation of cell growth.[20,22,23] However, fluorescent microscopy is a qualitative endpoint method that does not allow real-time analysis of metabolic behavior. There are a few examples of OOC with 3D functional tissues and built-in sensors. Some lab-on-chip assays depend on either electrochemical or optical-chemical sensing, and parameters, such as oxygen concentration,[24–26] pH level,[27,28] cell differentiation[29] or glucose consumption,[30] can be monitored to study cellular metabolism changes, but they do not provide specific information.[31] Our laboratory has fabricated modular platforms to detect specific biomarkers from complex biological media, such as insulin or interleukin-6 (IL6).[32,33] OOC integrated with new sensing technologies allows more straightforward cellular measurements across different tissues. For these reasons, in vitro devices for studying the cross-talk between different cell populations would help understand complex systems contributing to metabolic diseases.

To study the cross-talk between skeletal muscle and pancreatic islets under training conditions, we have bioengineered a new in vitro platform. Both muscle tissues and pancreatic islets have been generated and combined in a multi-organ-on-chip (multi-OOC) approach to study insulin secretion of pancreatic islets associated with the contraction of muscle tissues. In a multidisciplinary approach, we have used micro- and nanoscale fabrication technologies developed by our research group and

integrated novel biosensing technology to monitor cross-talk dynamics in real-time. Engineered tissues have benefited from novel scaffolds and have been integrated with bioreactors, an electrical stimulator, and biosensors to monitor myokine secretion from skeletal muscle cells, insulin production, and effects of skeletal muscle contraction on beta-cells. The proposed model addresses in vitro co-culture of the pancreas and skeletal muscle to go beyond the state-of-the-art 3D organ in vitro models. This multi-OOC is an important enabling step for diabetes modeling, the study of insulin resistance, and the investigation of drug candidates for therapy, usually performed by long-time and expensive animal experiments.

2. Results

2.1. Engineering Functional 3D Skeletal Muscle Tissue

We used a hydrogel molding technique to fabricate functional 3D skeletal muscle tissues (**Figure 1**A). Polydimethylsiloxane (PDMS) casting molds consisting of a well containing two pillars (Figure 1B) were used to encapsulate C2C12 myoblasts in a matrix of fibrin and Matrigel (Figure 1A). Hydrogel compaction is promoted by the matrix remodeling that started during the first hours after encapsulation, and tissues were detached entirely from the PDMS surface after 1 day (Figure 1C,D). Matrix remodeling is crucial in this casting mold fabrication process to implement uniaxial tension and promote self-organization of the cells through tissue formation (Figure 1C–F). After 2 days in growth conditions, samples were changed to differentiation medium to induce the myogenic program. The tissues were completely compacted between the two pillars of the casting mold after 7 days of encapsulation. Of note, 3D skeletal muscle tissues formed long multi-nucleated and aligned myotubes (Figure 1G–J). Remarkably, sarcomeric alpha-actinin immunofluorescence staining showed the presence of striations in the myotubes (Figure 1H), indicating the presence of mature sarcomeric structures in the 3D skeletal muscle tissues.

To evaluate the functionality of the 3D skeletal muscle tissues, the tissues were stimulated electrically (electric pulse stimulation, EPS) with a frequency sweep going from low to high frequencies. The displacement of casting mold pillars was measured to monitor the contraction dynamics of the skeletal muscle tissues during EPS (Figure 1K). Tissues showed a twitch contraction dynamic at low EPS frequencies. At high frequencies, the responses changed from twitch to tetanic-like dynamics. These results show that our 3D skeletal muscle tissues are mature and can respond to stimulation by contracting.

2.2. Carboxymethyl Cellulose-Based Scaffold Promotes MIN6 Pseudoislet Formation as a Model to Study Pancreatic Islet Function

Insulin-secreting mouse insulinoma-6 (MIN6) cells were seeded onto 3D carboxymethyl cellulose (CMC) scaffolds to generate pseudoislets as a model to mimic primary pancreatic islet morphology (**Figure 2**A). As we described previously,[16] CMC-based
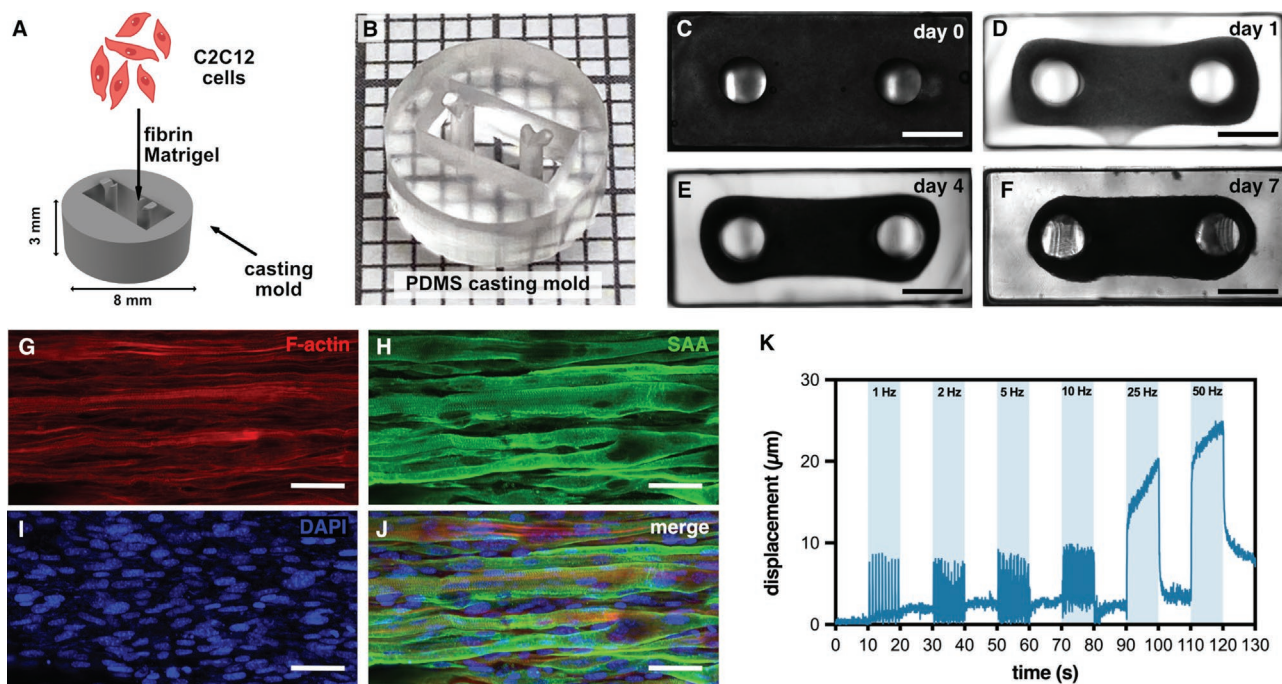
Figure 1. Bioengineered skeletal muscle responds to electric pulse stimulation. A) Schematic representation of C2C12 cells encapsulation in fibrin and Matrigel using PDMS casting molds. B) Photo of PDMS casting mold C–F) Representative top-view brightfield images of a skeletal muscle tissue compaction at different time points. Scale bars: 1 mm. G–J) Representative confocal images showing long, aligned myotubes in the bioengineered skeletal muscle tissue at day 7. G) F-actin is stained in red, H) sarcomeric α-actinin (SAA) in green showing striated patterned myotubes, and I) the nuclei were counterstained in blue with DAPI. Scale bars: 50 μm. K) Representative pillar displacement measurement line graphs obtained during electrical pulse stimulation (EPS) at different frequencies (i.e., 1, 2, 5, 10, 25, and 50 Hz) of a skeletal muscle tissue.

scaffolds promoted the formation of MIN6 aggregations, morphologically resembling primary pancreatic islets. Cytoarchitecture of pseudoislets was assessed by immunostaining and visualized under confocal microscopy (Figure 2B–D). The analysis of the proliferation marker Ki67 revealed that, after 1 day of seeding in the CMC-cryogel the MIN6 cells presented high a proliferation rate (8%) and that this ratio decreased over time, reaching 4% of cells proliferating at day 7 (Figure 2D). The size and shape of pancreatic islets are critical for the β-cell capacity to maintain their identity and to secrete insulin in response to glucose and other secretagogues.[34,35] To assess the gene expression profile of the MIN6 pseudoislets, we first evaluated genes encoding key transcription factors involved in the β-cell function, such as *MafA, Pdx1,* and *NeuroD1* (Figure 2F–H). Interestingly, on days 1, 4, and 7, even though it was not significant, the expression of these genes was upregulated compared to cells seeded in a plate. Additionally, the expression of *Atf3*, a gene involved in stress responses, presented a clear downregulation over time, and Ki67 showed a significant decrease in its expression on day 7 (Figure 2I,J), corroborating our previous results.[16]

The capacity to secrete insulin by the pseudoislets was evaluated by a glucose-stimulated insulin secretion (GSIS) assay. Briefly, cells seeded in a monolayer and pseudoislets were exposed to low glucose levels (2.8 mм [G3]) followed by high glucose concentration (25.5 mм [G25]). No significant differences were observed between cells seeded in a plate and CMC-based pseudoislets. In both conditions, MIN6 cells responded to the glucose challenge by secreting insulin, therefore

demonstrating that the functionality of the aggregated cells was maintained throughout the week. (Figure 2K–M). Collectively, these results show that encapsulated MIN6 cells within a 3D microporous scaffold maintain their β-cell identity and their capacity to secrete insulin and can be used as a suitable model to study β-cell-related diseases.

2.3. Development of a Microfluidic Multi-OOC Device for Tissue Engineering Applications

We developed a Multi-OOC device to accommodate, link, and analyze the cross-talk between the two biological models (i.e., the PDMS mold holding the skeletal muscle tissue and the CMC scaffold laden with pancreatic pseudoislets). This device consists of a PDMS microfluidic system with two open chambers to integrate the biological samples and a polymethyl methacrylate (PMMA) enclosure that seals the fluidic system. The modular approach using the enclosure allows us to grow both tissues independently and to connect them on demand for co-culture experiments fluidically. 2D computer-aided design (CAD) schematic drawings of the Multi-OOC, including all the parts and their dimensions, are shown in Supporting Information (Figure S3A, Supporting Information). Detailed information about fabrication is described in the Experimental Section. Briefly, the microfluidic chip (**Figure 3**A–D) consists of a PDMS multi-layer block (Figure S3C, Supporting Information) with fluidic channels and two tissue chambers, that is, a muscle chamber to host the 3D muscle tissue construct and a pancreas

2200873 (3 of 12)
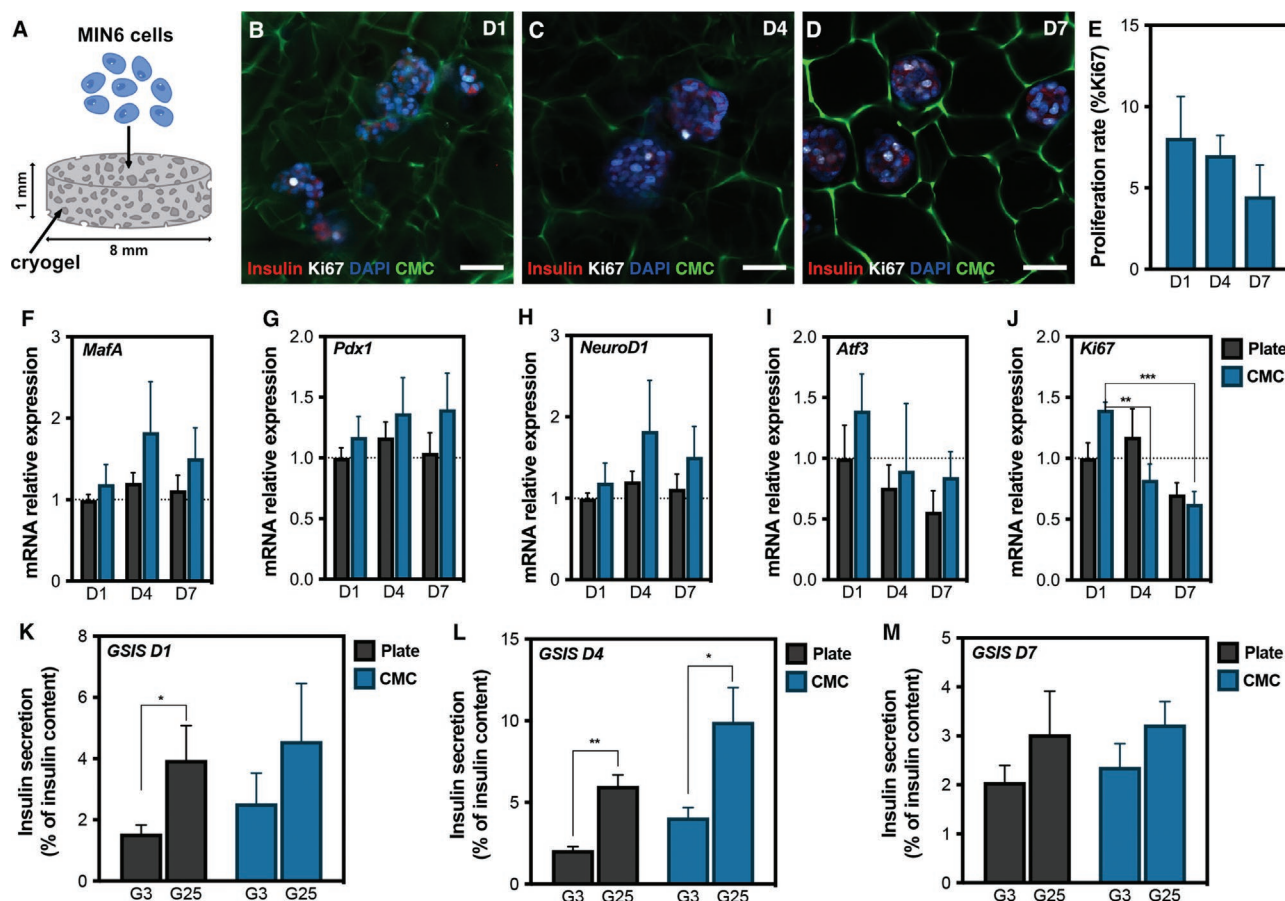
Figure 2. Pseudoislets generated in CMC-based cryogel scaffolds as a suitable model to study pancreatic islet function. A) Schematic representation of MIN6 cells seeding in microporous CMC-based cryogel scaffolds. B–D) Round-shaped pseudoislets generated within a 3D microporous scaffold. MIN6 cells are stained for insulin (red), Ki67 (white), and nuclei (DAPI). Aminofluorescein was used to stain the fibers of the cryogel (green). Scale bar = 100 µm. E) Proliferation rate (calculated as the percentage of Ki67-positive β-cells among the total number of β-cells) of MIN6 cells inside the CMC-cryogel. F–J) Gene expression analysis of MafA, Pdx1, NeuroD1, Atf3, and Ki67. Data are shown relative to cells seeded in a plate on day 1. Results are normalized against Tbp1 and are expressed as the mean and SEM. **$p < 0.01$, ***$p < 0.001$. K–M) Glucose-stimulated insulin secretion (GSIS) assay on days 1, 4, and 7 comparing cells seeded in a plate (monolayer) and cells seeded within a CMC-based cryogel (pseudoislets). Insulin secretion is assessed at basal levels of glucose (2.8 mM [G3]) and after a challenge of glucose stimulation (25.5 mM [G25]). Results are expressed as the percentage of insulin secreted with respect to total insulin content. *$p < 0.05$, **$p < 0.01$, ***$p < 0.001$ ($n = 6$).

chamber to host the CMC scaffold containing MIN6 pseudoislets (See Figure 3B). These two engineered models are placed manually into the PDMS chip, which is later assembled and sealed using an external PMMA case (Figure S3E, Supporting Information).

The fluidic system was assembled using silicone tubing (0.8 and 1.6 mm inner and outer diameter, respectively), which connected the inlet and outlet of the microfluidic device to a reservoir and a peristaltic pump, respectively. By withdrawal pumping, the culture media flows from the reservoir to the microfluidic chip (muscle tissue chamber first and pancreas chamber later) and is finally discarded in a waste container. Culture media distribution throughout the microfluidic chip was numerically computed using COMSOL Multiphysics software. Velocity distribution for a flow rate of 50 µL min⁻¹ at the plane of the fluidic channels is shown in Figure 3E, including detailed distribution and direction of the flow in both chambers (Figure 3F,G). An additional animation with the fluid velocity at different parallel planes is depicted in

Movie S2, Supporting Information. The flow rate condition of 50 µL min⁻¹ in our system permits the concentration of substrates near the samples while enabling a rapid fluidic communication between the two tissues and renovation of media in the chambers, whose volumes are 157 and 314 µL for the muscle and pancreas chambers, respectively. Same velocity distribution representations are provided in Figure S2A, Supporting Information for other flow rates (i.e., 10, 100, and 200 µL min⁻¹). At a flow rate of 50 µL min⁻¹ this flow rate, the predicted calculated shear stress was <0.003 dyn cm⁻² surrounding the skeletal muscle tissue, and <0.0006 dyn cm⁻² on top of the pseudoislets tissue (Figure S2B, Supporting Information).

To perform EPS of the muscle tissue (Movie S3, Supporting Information), the upper PMMA cover includes two 6 mm pitch graphite electrodes (4 mm in width and 1 mm in thick) that fit into the muscle chamber (Figure S4A, Supporting Information). Electrochemical impedance spectroscopy measurement between the two electrodes (Figure S4B, Supporting Information)
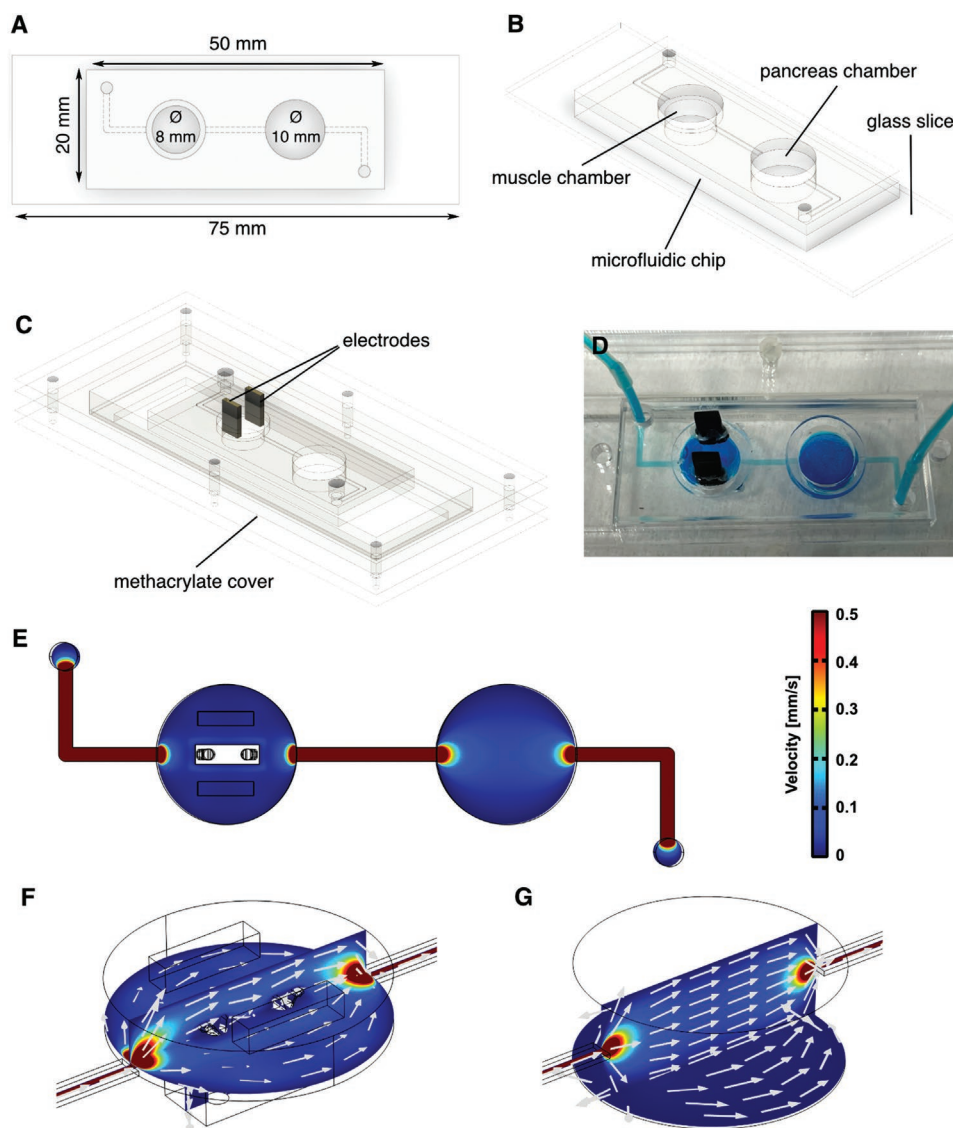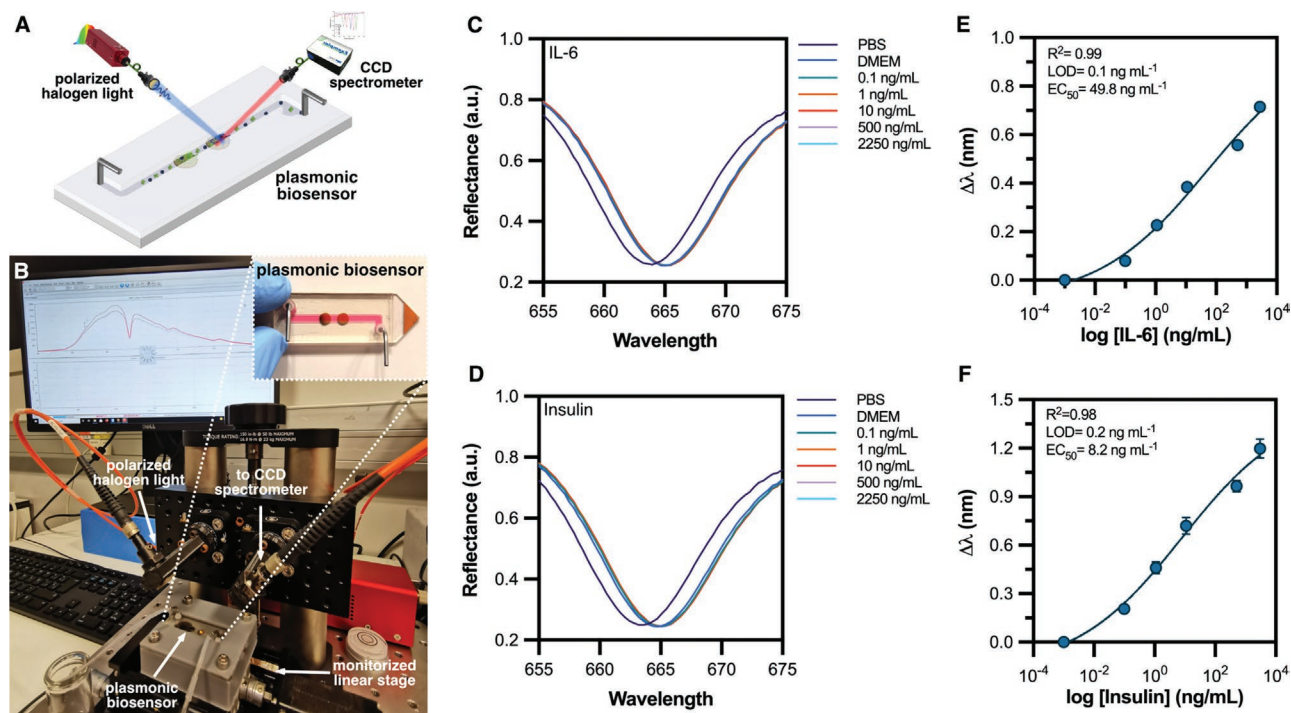
Figure 3. Design and fabrication of the microfluidic Multi-OOC device. A–C) Schematic drawings showing the dimensions and assembly of the Multi-OOC device. D) Photograph of the Multi-OOC device assembled. Note that a blue dye was used for a visualization of the channels and chambers. Numerical study of the flow velocity performed with COMSOL Multiphysics software using a flow rate condition of 50 µL min⁻¹ at the inlet. Simulation images include the flow velocity E) throughout the microfluidic chip (plane at the microfluidic channels) and F) inside the muscle and the G) pancreas chambers (parallel plane 0.1 mm above the tissue and orthogonal plane). Grey arrows indicate direction of the media in both chambers.

confirms that the tissue can be subjected to an electrical stimulus of 1 ms of pulse width without electrical loss and electrochemical reactions at the electrode-electrolyte interface. Due to the particular geometry of the system (i.e., chamber, electrodes, and tissue), the electric field applied along the tissue was numerically calculated using COMSOL Multiphysics software. A 3D plot of the tissue with a colormap of the electric field magnitude is represented in Figure S4C, Supporting Information. In addition, the electric field profile along the three orthogonal axes is shown in Figure S4D, Supporting Information. According to these numerical results, the electrical field is uniformly applied along with the whole tissue with an average electric field magnitude of 1 V mm⁻¹ and mainly along the lateral axis of the tissue.

2.4. Development of Plasmonic Biosensing Platform Based on Nanogratings Structured Surface

Plasmonic biosensors were developed by a high-throughput fabrication process using Blu-Ray optical discs as polymeric templates containing nanogratings (Figure S5A, Supporting Information). The bared polymeric nanogratings were coated with a thickness optimized thin gold layer for enhanced protein-antibody biorecognition events. Later, the plasmonic chips were integrated with microfluidics using a patterned double-sided adhesive tape and a PMMA lid with inlet/outlet ports.

The integrated sensors were placed on a custom-made reflectance experimental setup at 40° (**Figure 4**A,B) with linearly polarized transverse magnetic (TM) mode light for sensor

**ADVANCED
SCIENCE NEWS**

www.advancedsciencenews.com

**ADVANCED
MATERIALS
TECHNOLOGIES**

www.advmattechnol.de

Figure 4. IL-6 and insulin plasmonic biosensor. A) Schematic representation of the multiplexed plasmonic biosensor for IL-6 and insulin secretion monitoring. B) Photograph of the experimental setup (plasmonic sensing platform) including the optical detection scheme and the microfluidic system. Plasmonic peak displacement with different concentrations of C) IL-6 and D) Insulin spiked cell culture media in an additive assay respectively. Calibration curve for the detection of E) IL-6 and F) insulin in cell culture media respectively ($n = 2$).

characterization. In the first step, HCl solutions with different refractive indexes were flown through the sensor to estimate the bulk refractive index sensing performance of the plasmonic sensor. The bulk sensitivity was estimated by measuring the wavelength displacement of the plasmonic band with refractive index changes (Figure S6C, Supporting Information). There was a linear response of the wavelength displacement of the plasmonic band with the changes in refractive index and estimated bulk sensitivity of the sensor ≈ 336 nm/RIU was achieved (Figure S6D, Supporting Information). Finally, ten random sensor chips from three different fabrication processes were tested in aqueous media, and their reflectance spectra were recorded for reproducibility analysis. A coefficient of variation under 1% was observed in the plasmonic band peak centroid (664.47 ± 0.53 nm) between the ten sensor chips (Figure S6E,F, Supporting Information). Plasmonic sensor chips selected for biosensing experiments were characterized as previously described and presented an average refractometric sensitivity of 336.9 nm/RIU with a coefficient of variation between them of below 2% (Figure S6G, Supporting Information).

To immobilize IL-6 and insulin antibodies on the nanograting surface, the plasmonic sensors were modified by forming a self-assembled monolayer (SAM) with carboxylic groups (−COOH). Next, activating the carbodiimide chemistry resulted in an NHS ester intermediate highly reactive to primary amines (NH2) present in the antibodies (Figure S5B, Supporting Information). The immobilization was performed ex situ. The detection of different concentrations of IL-6 and insulin proteins spiked in DMEM cell culture media (from 0.1 to

2250 ng mL^{-1}) showed an excellent spectral evolution under additive assays (Figure 4C,D). We achieved limits of detection (LOD) of 0.01 and 0.02 ng mL^{-1} for IL-6 and insulin, respectively. Half maximal effective concentration (EC50) values of 49.8 and 8.2 ng mL^{-1} for IL-6 and insulin were estimated, respectively (Figure 4E,F). No cross-reactivity was observed between the proteins (Figure S6A,B, Supporting Information).

2.5. Training-on-a-Chip Integration for the Real-Time and Multiplexed Monitoring of IL6 and Insulin Secreted Levels

Training-on-a-chip experiment was set up integrating the Multi-OOC with the plasmonic biosensing platform to monitor in real-time the cross-talk effect of the IL-6 secreted by an electrically stimulated skeletal muscle tissue over the insulin secretion of the pseudoislets, simulating the native pancreas model (**Figure 5**A,B). The Multi-OOC device containing both tissues was placed inside a portable incubator to maintain the culture conditions during the experiment. The reservoir with sterile cell culture media used during the experiment was also kept inside the incubator under the same conditions. To perform the EPS regime stimuli, the graphite electrodes from the Multi-OOC device were connected to the arbitrary wave generator. To connect the Multi-OOC device inside the incubator to the PSP a tubing network was used. Of note, a T-connector was located at the entrance of the PSP to allow the exchange of the sensors eliminating the bubbles in the system. To deliver the cell culture media containing the secreted targets from the Multi-OOC
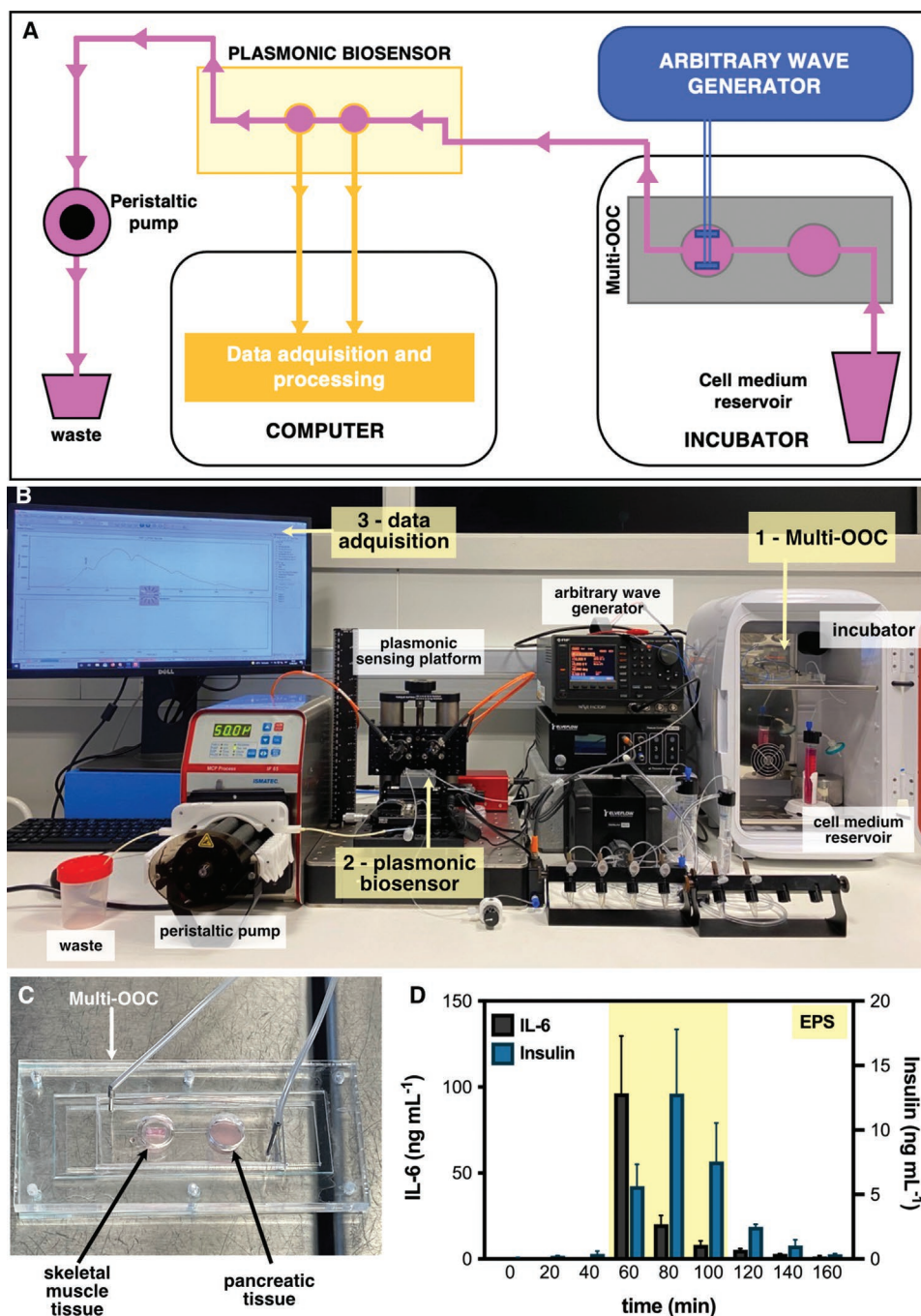
Figure 5. IL-6 and insulin are secreted as response to muscle contraction induced by EPS. A) Schematic representation of experimental setup. B) Picture of the experimental setup integrating the Multi-OOC device with the plasmonic sensing platform. C) Multi-OOC showing the skeletal muscle and pancreatic tissues located in their respective chambers. D) Online monitoring of IL-6 and insulin detection acquired by the plasmonic sensing platform during the EPS experiment. Skeletal muscle tissue was electrically stimulated between 60 and 120 min in the experiment (yellow band).

to the PSP, a peristaltic pump on reverse mode and with a flow rate of 50 µL min^{-1} was used. Finally, the multiplexed detection in real-time was performed in the PSP, and data acquisition was collected in real-time monitoring the plasmon changes.

The cell culture media from the Multi-OOC was analyzed every 20 min step under continuous flow mode. A biosensor was replaced every 20 min to avoid signal saturation. The

optical properties of each sensing platform used during this experiment were previously evaluated, demonstrating the high reproducibility (Figure S5E,F, Supporting Information). The detection monitoring was performed from 0 to 40 min, simultaneously detecting IL-6 and insulin secretion from the muscle and pancreas chamber (Figure 5C). Then, both analytes were monitored under EPS conditions for 60 min (See yellow

**ADVANCED
SCIENCE NEWS**

www.advancedsciencenews.com

**ADVANCED
MATERIALS
TECHNOLOGIES**

www.advmattechnol.de

range in Figure 5D). After 60 min of electrical stimulation, the wave generator was stopped, and the monitoring continued over 1-h post-stimuli conditions. The optical response obtained was converted into quantitative analysis for IL-6 and insulin using the calibration curves previously obtained (Figure 4E,F).

A basal expression below 0.5 ng mL^{-1} for IL-6 and insulin was detected before the EPS stimulus. However, IL-6 values increased dramatically as a response to EPS during the first 20 min, and their levels decreased during that time. A maximum of 96 ng mL^{-1} of IL6 was detected during the first 20 min of electrical stimulation. Interestingly, an insulin secretion increment was detected as an initial response to the muscle contraction induced by EPS during the first 20 min, and their levels increased after IL-6 secretion during the time. The maximum secretion of insulin (13 ng mL^{-1}) was detected after 40 min of electrical stimulation of the muscle tissue. In both cases, insulin and IL-6 secreted levels decreased to basal levels once the EPS was stopped, demonstrating that both proteins are secreted as a result of muscle contractions. To confirm these data, we cultured MIN6 pseudoislets with conditioned medium from skeletal muscle tissue after 1 h of EPS and monitored insulin secretion. Insulin levels increased time-dependent in response to the EPS-stimulated skeletal muscle tissue conditioned medium (Figure S7A, Supporting Information). Finally, to assess whether insulin secretion is mediated by muscle IL-6, pseudoislets were cultured with a medium supplemented with 100 ng mL^{-1} of IL-6 under high glucose concentration. In line with the above results, insulin secretion increased in a time-dependent manner as a result of IL-6 stimuli (Figure S7B, Supporting Information). Altogether, these results confirm the potential of the Training-on-a-Chip to study insulin secretion as a response to muscle contraction in vitro.

3. Discussion

The effect of exercise on lowering blood glucose levels has been widely tested.[36] However, traditionally it has been attributed to an enhanced muscle glucose uptake and increased insulin sensitivity in peripheral tissues. In the last decade, several studies have pointed out that exercise may improve the secretory capacity of beta-cells in patients with T2D.[37,38] However, the traditional models used to date do not allow us to discern whether insulin secretion is directly mediated by paracrine signaling in the muscle fibers or other cell types. On the one hand, in vivo physiological studies in humans or animal models make it possible to study the effect of exercise on insulin secretion, but not to determine whether the effect is due to muscle contraction or any other organ mediating this signaling. On the other hand, in vitro studies using traditional 2D cultures do not allow real-time analysis of the cross-talk between muscle and pancreatic beta-cells.[39] To overcome these constraints, in this work we have developed a dynamic model to study how muscle contractions signal pancreatic beta-cells in real-time.

In vitro systems that mimic organ and tissue microarchitecture have been demonstrated to be superior to conventional 2D models. Combining multiple sophisticated models and sensing capabilities is expected to result in more reliable models with translational potential. However, this advanced integration demands the utilization of diverse and complex technologies that are usually difficult to combine. Here we have bioengineered two 3D constructs for skeletal muscle and pancreatic cells that recapitulate their physiological tissue organization: suspended muscle fibers encapsulated in an extracellular matrix and spherical pancreatic pseudoislets. Using a modular approach, we created a multi-tissue model—called training-on-chip—for testing exercise-induced insulin secretion. This approach permitted the separate maturation of the tissues so that we could apply particular culture conditions for their formation before their co-culture into the device. Paracrine signaling between both tissues was later enabled by employing microfluidics, while integrated biosensors allow us to quantify the profile of IL-6 and insulin released in situ. To prove its feasibility, we challenged skeletal muscle cells with a transitory exercise-like stimulus and monitored the direct effect of skeletal muscle contraction on pancreatic beta-cells. We detected a rapid secretion of IL-6 in response to muscle contraction, while insulin secretion by pancreatic islets was secondary to muscle contraction with a delay of a few minutes. The effect of muscle contraction on insulin secretion was recently described.[39] However, these studies were based on the use of conditioned media from muscle to challenge the β-cell cultures in a static assay 2D standard culture. Of note, our training-on-a-chip device has made it possible to study this cross-talk in real-time and determine the signaling dynamics between the two 3D tissues.

For the first time, we have developed a multi-OOC platform to monitor the cross-talk between two organs in real-time with high sensitivity and in a multiplexed way. Previous works have been presented integrating sensing elements into microfluidic systems. However, they are based on sensing platforms that do not allow real-time monitoring of the outputs.[40,41] In previous work, we implemented a microfluidic sensing device to mimic the functionality of primary mouse pancreatic islets.[42] This system integrated a sophisticated optical biosensing platform to monitor the insulin secretion by pancreatic islets in real-time. Nevertheless, the fabrication process of this system had a high cost, the sensing platform did not allow multiplexing, and the operation of the device was very complex (i.e., the readout setup and the microfluidic platform). Altogether, these issues make applying that sensing system application in a multi-OOC cross-talk study difficult. Conversely, in the present work, we developed a sensing platform coupled with the multi-OOC device with several advantages compared to the previously reported sensing systems.[43–45] These advantages include a cost-effective manufacturing method, the dispensability for labeled antibodies, easy connection with the OOC devices, multiplexing, and the capability of monitoring in real-time. Remarkably, the multiplexing quantification with high sensitivity (limits of detection of 0.01 and 0.02 ng mL^{-1} for IL-6 and insulin, respectively) of secreted proteins due to the tissue cross-talk is a unique and novel feature presented in this work. This is critical to understanding the physiologic relationships between the skeletal muscle and the pancreas, two of the main organs involved in T2D.

The platform developed in this work is suitable for maintaining the tissues in terms of housing and providing optimal conditions for culture and analysis. Materials are biocompatible with hosting the tissues and primarily were designed to study

**ADVANCED
SCIENCE NEWS**

www.advancedsciencenews.com

**ADVANCED
MATERIALS
TECHNOLOGIES**

www.advmattechnol.de

an electrically stimulated skeletal muscle tissue and its effect on bioengineered pancreatic islets. Nevertheless, the platform is versatile and could be used to host and study the cross-talk of other types of organs. The future applications of this platform are promising, especially this focused on disease modeling, drug screening, and personalized medicine.

4. Experimental Section

Cell Culture: Murine C2C12 myoblasts (American Type Culture Collection (CRL-1772)) were cultured in DMEM with 4.5 g L^{-1} glucose (Gibco, Thermofisher), 1% penicillin-streptomycin (10 000 U mL^{-1}) P/S (Gibco, Thermofisher), and 10% fetal bovine serum (FBS) (Gibco, Thermofisher). Insulin-secreting mouse insulinoma-6 cells (MIN6) were kindly gifted by Dr. Joan Marc Servitja (Diabetes and Obesity Research Laboratory, IDIBAPS, Spain). MIN6 cells were grown with DMEM 4.5 g L^{-1} glucose (Gibco, Thermofisher), supplemented with 10% FBS (v/v), 2 mmol L^{-1} glutamine (Gibco, Thermofisher), 1% penicillin-streptomycin (10 000 U mL^{-1}) P/S, and 50 µmol L^{-1} β-mercaptoethanol (Gibco, Thermofisher). Cells were kept in a humidified cell culture incubator in a 5% CO_2 atmosphere at 37 °C. When cells reached 70% confluence, they were trypsinized and split by seeding 5×10^5 cells into new culture 175 cm^2 flasks. C2C12 cells were used up until passage number 8. Co-culture of skeletal muscle tissue and pancreatic pseudoislets in the multi-OOC were cultured in DMEM 4.5 g L^{-1} glucose (Gibco, Thermofisher), supplemented with 10% FBS (v/v), 2 mmol L^{-1} glutamine (Gibco, Thermofisher), 1% penicillin-streptomycin (10 000 U mL^{-1}) P/S, and 50 µmol L^{-1} β-mercaptoethanol (Gibco, Thermofisher).

Muscle Casting Molds Design and Fabrication: PDMS molds for encapsulating myoblasts were generated from replica molding using a 3D positive resin and negative silicone molds (Figure S1, Supporting Information). The positive mold with 10 replicas of the muscle casting molds was designed with the Autodesk Fusion 360 software (Autodesk Inc). The positive resin mold was fabricated with a digital light processing (DLP) 3D printer (Solus DLP 3D printer, Reify3D) and Solus Proto resin. For easily demolding of the final PDMS casting molds, the rigid mold was used to generate negative replica molds in a soft silicone material Ecoflex silicone (Ecoflex 00-30, Smooth-On Inc.). Casting with Ecoflex silicone enabled the high-throughput fabrication of PDMS molds. Ecoflex negative replica mold was generated by pouring pre-polymer mix (1A:1B) on the 3D printed positive mold. Ecoflex was left cured at room temperature overnight after degassing for 15 min in a vacuum desiccator. Finally, Ecoflex negative replica mold was washed with EtOH, rinsed dry with compressed N2 flow, and let dry on a hot plate for 10 min at 90 °C. Next, to generate the individual muscle casting molds, PMDS prepolymer was mixed with the curing agent 10:1 w/w ratio, first degassed for 10 min, and then poured directly on the Ecoflex mold. Subsequently, the air from the pillars was removed with a syringe to facilitate the insertion of the elastomer in the pillars and a second 20 min degassing step was applied. PDMS was cured for 6 h at 80 °C and the casting molds were taken out of the Ecoflex mold. To facilitate the demolding processes, both the 3D printed positive mold and the negative Ecoflex replica mold were coated with trichloro(1H, 1H, 2H, 2H-perfluorooctyl)silane (PFOTS) using chemical vapor deposition. Finally, a round crystal coverslip (8 mm) was bonded to the bottom of the individual casting mold by activation of the two surfaces, bottom of the casting mold and crystal, in an UV-Ozone plasma cleaner (ProCleaner Plus, BioForce Nanosciences) for 15 min.

Bioengineered Skeletal Muscle Fabrication: C2C12 cells were encapsulated at 5×10^7 cells mL^{-1} in a cell/hydrogel mixture of 30% v/v Matrigel Basement Membrane Matrix (Corning), 4 mg mL^{-1} fibrinogen from human plasma (Sigma Aldrich), and 2 U of thrombin from human plasma (Sigma Aldrich). 35 µL of the mixture was pipetted within each PDMS casting mold using cool tips to avoid premature polymerization.

The cell/hydrogel mixture was polymerized for 30 min at 37 °C followed by incubation in growth medium containing 1 mg mL^{-1} of

6-aminocaproic acid (ACA) (Sigma Aldrich). They were kept in growth media for 2 days and then switched to differentiation medium containing 1 mg mL^{-1} of ACA for 7 days. Half of the volume of the differentiation medium (DMEM, 2% horse serum, 1% P/S) was replaced every 2 days.

Fluorescence Methods and Imaging: Bioengineered tissues were immunostained as previously described elsewhere.[16,46] Briefly, tissues were fixed for 30 min at room temperature (RT) in 10% formalin solution and permeabilized with PBS-T (0.1% Triton-X in PBS) Samples were blocked for 2 h at RT using blocking solution (0.3% Triton-X, 3% donkey serum in PBS) and incubated with primary antibodies (Table S1, Supporting Information) at 4 °C overnight. After several PBST washes, the samples were incubated for 2 h with the fluorophore-conjugated secondary antibody (Table S1, Supporting Information) at RT. Finally, the samples were counterstained with DAPI (Life Technologies) to detect the nuclei and RhodamineB-phalloidin (Life Technologies) to label the actin cytoskeleton. Fluorescence images were taken with a ZEISS LSM800 confocal laser scanning microscope. Top-view images and videos of 3D skeletal muscle tissues were taken with a ZEISS Axio Observer Z1/7 microscope. Both images and videos were analyzed using the Fiji image processing package, a distribution of Image J.[47]

EPS: EPS was applied on day 7 after induction of myogenic differentiation of the bioengineered skeletal muscle tissues. The stimulation was performed by placing the tissues either inside a homemade stimulation plate with electrodes or into the multi-OOC device and electrically connecting the electrodes to a multifunction generator (WF 1948; NF Co.). A train of monophasic pulses (frequency of 1 Hz, amplitude of 10 V, and pulse width of 1 ms) was applied between the two graphite electrodes for 1 h. The mean electric field generated throughout the tissue was 1 V mm^{-1} according to a numerical study considering the dimensions of the chamber and the localization of the tissue therein (Figure S4, Supporting Information).

Cryogel Fabrication and Cell Seeding: 1% CMC (Sigma Aldrich) scaffolds were fabricated as described elsewhere.[48] Once cryogels were fabricated, they were dried for 30 min and 200.000 insulin-secreting mouse insulinoma-6 (MIN6) cells were seeded in each cryogel. Cells were maintained at 37 °C and 5% CO_2 in DMEM (25 mmol L^{-1} glucose) supplemented with 10% FBS (v/v), 2 mmol L^{-1} glutamine, 100 units mL^{-1} penicillin, 100 µg mL^{-1} streptomycin, and 50 µmol L^{-1} β-mercaptoethanol.

GSIS: Cryogels containing MIN6 cells were preincubated with Krebs-Ringer bicarbonate HEPES buffer solution (115 mM NaCl, 24 mM NaHCO₃, 5 mM KCL, 1 mM MgCa₂ × 6H₂O, 1 mM CaCl₂ × 2H₂O and 20 mM HEPES, pH 7.4) at 2.8 mM glucose for 30 min. Then, cryogels were incubated at low glucose (2.8 mM) for 1 h, followed by incubation at high glucose (25 mM). After each incubation step, supernatants were collected and total insulin content was recovered in acid-acetic lysis buffer (glacial acetic acid 5.57%). Insulin concentration was determined by ELISA (Crystal Chem) following the manufacturer's instructions.

Gene Expression Analysis: RNA was extracted using the miRNeasy kit (Qiagen), and retrotranscribed using the SuperScript Reverse Transcriptase kit (Life Technologies). Quantitative PCR reactions were run using SyberGreen (Invitrogen) in a Step-One real-time PCR System (Thermofisher). Table S2, Supporting Information lists the primer sequences. *Tbp1* was used to normalize the mRNA expression of genes of interest.

Multi-OOC Device Design and Fabrication: Multi-OOC was fabricated using soft photolithography methodology using the negative photoresist SU8-2100 (MicroChem). The microfluidic chip was initially designed with CleWin 5 and then printed on a high-quality acetate film to be used as a mask. Silicon wafers substrates (4" n-type <111>, MicroChemicals GmbH) were cleaned in a oxygen plasma chamber (PCD-002-CE, Harris Plasma Cleaner) for 20 min at 6.8 W. The SU-8 master was then obtained by contact photolithography using a Mask aligner (SÜSS Microtec, MJB4) 240mJ cm^{-2} energy radiation at 365 nm followed by the respective developing and baking processes. Finally, SU-8 patterned substrates for fabrication of PDMS (poly-dymethyl-siloxane, Sylgard Elastomer base, and curing agent) molds were obtained. As a final step, silicon molds had to undergo silanization for obtaining hydrophobic surfaces to avoid

**ADVANCED
SCIENCE NEWS**

www.advancedsciencenews.com

**ADVANCED
MATERIALS
TECHNOLOGIES**

www.advmattechnol.de

permanent bonding with polymer. Two layers of PDMS were fabricated. First layer contains the microfluidic network from the silicon wafer previously prepared and the second layer of PDMS was used to have the microfluidic channels at the same height as the chamber where tissue was located, thus improving the distribution of the medium across the chambers (Figure S3C, Supporting Information).

To create the PDMS resin the polymeric base was mixed with the curing agent (Sylgard 184, Dow corning) in a ratio of 10:1 (w/w). The PDMS was degasified in a vacuum desiccator for 1 h to remove the air bubbles and finally poured on the SU-8 master mold. The PDMS was then cured in an oven at 80 °C for 2 h and left overnight at room temperature. Once cured, it was peeled from the mold, cut, and followed by a hole punch process to make the tissue chambers holes, inlets, and outlets. The two PDMS layers were activated using O_2 plasma at 45 W for 30 s (PCD-002-CE; Harrick plasma cleaner) and irreversibly bonded together. The resulting 5 mm thick PDMS slab was treated again with O_2 plasma and bonded to a 75×25 mm glass slide to support it. Two polymethyl methacrylate (PMMA) plates (3 mm in thickness) were cut using a CO_2 laser engraver (Epilog Mini 24, Laser Project) and milled with a milling machine (Roland MDX-40, Roland DG Iberia) to enclose the PDMS device (external case). The upper PMMA plate serves to position the graphite electrodes and seal the fluidic system, whereas the lower plate enables alignment of the PDMS device. To assemble the fluidic system, the three parts (i.e., PDMS device and lower and upper PMMA plates) were fixed in place by means of nylon screws. The general dimensions of the Multi-OOC device and the PMMA case are shown in Figure S3, Supporting Information. The microfluidic chip (Figure 3A–D) consists of two (3 and 2 mm thick) 50×20 mm PDMS layers (Figure S3C, Supporting Information). First, an 8 mm hole (inner well) was punched in a 3 mm PDMS bottom layer to host the 3D skeletal muscle tissue construct. A second 2 mm thick PDMS layer (upper layer) was replicated from a silicon master containing the microfluidic channels and bound irreversibly to the bottom layer. Then, two holes of 10 mm in diameter were punched in the PDMS slab to form both tissue chambers, that is, a muscle chamber to host the 3D muscle tissue construct and a pancreas chamber to host the CMC scaffold containing MIN6 pseudoislets (See Figure 3B). Both chambers, together with the inlet and outlet, were connected through a rectangular microfluidic channel (1 mm width and 0,2 mm height). Finally, the PDMS layers were bound irreversibly to a $70 \times 25 \times 1$ mm glass slide. To seal both chambers that were open in the microfluidic device, an external PMMA case including upper, middle, and lower covers, was designed by CAD software and fabricated using a milling machine. Schematic drawings of the PMMA case and its assembly with the microfluidic device are provided in Figure S3, Supporting Information. As a final step, the two engineered models were placed manually into the PDMS chip and later assembled and sealed with the external PMMA case using nylon screws (Figure S3E, Supporting Information).

COMSOL Simulations: Flow rate along the microfluidic device and electric field inside the tissue chamber were numerically analyzed using Finite Element Software (COMSOL Multiphysics version 5.4). The flow distribution along the microfluidic chip including both chambers was estimated using a laminar flow model and different conditions of flow rate (10, 50, 100, and 200 μL min^{-1}) at the microfluidic inlet. The 3D model was simulated with a mesh of 3.2×10^6 elements. The fluid velocity was evaluated to determine the optimal flow rate to link and homogeneously supply both tissues. The perfused media was selected to mimic the physical properties of DMEM supplemented with 10% FBS at 37 °C, that is, a density of 1.009×10^3 kg m^3 and dynamic viscosity of 0.93×10^{-3} Pas.[49] Otherwise, the electric field was calculated to evaluate its uniformity and magnitude along with the tissue. The electric field generated on the tissue was computed using the electrical currents interface of the AC/DC module. A 3D model of the chamber, including graphite electrodes and tissue, was developed with a tetrahedral mesh of 5.6×10^5 elements. To emulate the tissue, a cuboid of dimension $4 \times 1 \times 0.5$ mm was located just in the upper part of the PDMS posts. The electrical conductivity of the media was 1.5 S m^1 and the relative permittivity was 78. A potential difference of 10 V was applied between the two electrodes, which were spaced 5 mm (distance from edge to edge) and had the physical properties of graphite material (electrical conductivity of 3×10^3 S m^{-1}).

Fabrication and Integration of the Plasmonic Nanogratings Chip: The fabrication of the plasmonic biosensors was performed according to the previous reports.[50] Commercial Blu-ray discs (43743, Verbatim) were used as polymeric nanotemplates after removing the protective (thin polycarbonate) and reflective (aluminum) films. These films were removed by trimming the discs into individual substrates (size 5.6 cm^2) and then chemically etched using a hydrochloric acid solution (2 M HCl) for at least 12 h. Bared polymeric nanotemplates were then rinsed with MiliQ water and nitrogen dried. The sensing regions of the chips were patterned using an adhesive vinyl stencil sheet (250 microns) as an evaporation mask and finally placed in a vacuum deposition system (Univex 450B, Oerlikon). A thin layer of gold (70 nm) was deposited by resistive thermal evaporation (1 Å s^{-1}). A microfluidic reaction chamber for flow biodetection was fabricated by patterning a microfluidic channel into a double-sided adhesive tape foil (Mcs-foil-008, Microfluidic ChipShop GmbH). The proposed design integrates two sensing areas to allow multiplexed biosensing. A 2 mm thick polymethyl methacrylate (PMMA) lid with inlet and outlet ports allows the fluidic connection.

The sensors were fixed into a custom-designed reflectance experimental set-up. The sensors were connected to a microfluidic circuit with a pressure pump (OB1 Mark I, Elveflow) that allows precise control of flow speed. Optical measurements were performed under reflectance at a fixed angle (40°) with TM-polarized light from a UV-NIR light source (SLS201L, Thorlabs) at a perpendicularly aligned to nanograting direction excitation plane. The reflected light was collected by a charge-coupled device spectrometer (Exemplar UV-NIR, BWTek). Reflectance spectra were acquired every 1 ms with 50 consecutive averaged spectra to provide the final spectrum. These selected acquisition parameters allowed to obtain the optimal signal-to-noise (S/N) ratio without a long data acquisition time. Changes in the plasmonic band position (λ_{SPR}) were tracked via peak analysis using Origin 2018 software (OriginPro, OriginLab Co.).

Surface Biofunctionalization of Plasmonic Nanogratings and Antibody Detection Assays: Gold sensors were pretreated prior to surface biofunctionalization by performing a cleaning with consecutive rinsing with ethanol and MiliQ water, nitrogen drying, and finally treated in a UV ozone plasma cleaner (BioForce Nanoscience) for 20 min. The cleaned sensors were coated with an alkanethiol self-assembled monolayer (SAM) with reactive carboxylic groups by immersing the sensors in a 2.5 mM MUA (11-mercaptoundecanoic acid, Merck) ethanolic solution for at least 12 h at room temperature. Later, the sensor was rinsed with ethanol and MES buffer.

The immobilization of insulin and interleukin-6 monoclonal antibodies was performed by drop-casting. The carboxylic groups present in MUA were activated with a solution of 0.2 M EDC (1- ethyl-4 (3-dimethylaminopropyl) carbodiimide hydrochloride, Merck)/0.05 M Sulfo-NHS (Sulfo-N hydroxysuccinimide, Merck) in (2-ethanesulfonic acid) MES buffer (25 mM pH 5.7) for 40 min. The activated surface was rinsed with MES buffer, and 50 μg mL^{-1} of Mouse insulin (NB100-73008, Novus Bio) and interleukin-6 (554400, BD Pharmingen) antibody solution in (phosphate buffer) PB (10 mM pH 7.4) was dropped for 120 min. Then, the unreacted remaining active carboxylic groups were blocked by dropping an ethanolamine solution 50 mg mL^{-1} prepared in PB 10 mM pH 7.2 for 15 min. Subsequently, washing steps with PBS and PBS + 0.5% BSA were performed to rinse unbounded molecules and to fill non-specific binding sites. Finally, the sensors were nitrogen dried and bonded to the microfluidics, fixed in the experimental reflectance set-up, and flowed with PBS for assessment studies.

Calibration curves were performed by flowing over the sensors, different protein concentrations (IL-6 protein, (200-02, Shenandoah Biotech) and insulin protein (r91077C, Merck) diluted in DMEM cell culture media at 50 μL min^{-1}. Data points for each concentration were collected 20 min after injection. The resultant curves were fitted to a one-site specific binding model.

Statistical Analyses: Data were expressed as the mean ± SEM. At least 3 replicates were performed in each experiment. Pairs of samples were

**ADVANCED
SCIENCE NEWS**
www.advancedsciencenews.com

**ADVANCED
MATERIALS
TECHNOLOGIES**
www.advmattechnol.de

compared using a two-tailed Student t-test ($\alpha < 0.05$), applying Welch's correction when necessary. Multiple comparisons were analyzed by one-way ANOVA with a post-hoc Tukey test as appropriate. Statistical analyses were performed with GraphPad Prism Software V.9. Results were considered significant at $p < 0.05$. The standard curves were fitted to a four-parameter equation according to the following formula: $Y = [(A - B)/1 - (x/C)D] + B$ where A is the maximal signal, B is the minimum, C is the concentration producing 50% of the maximal signal, and D is the slope at the inflection point of the sigmoid curve. The calculation of the limit of detection (LOD) was based on immunoassay methodology.[51] For a standard curve, the LOD was the concentration corresponding to the interpolated intersection of the 10% confidence interval of the lower asymptote with the four-parameter equation fit of standards data. The EC50 was considered as the concentration of a compound where 50% of its maximal signal was achieved. The software used for this fitting and statistics was GraphPad Analysis Software using a dose-response four-parameter fitting model. All the measurements were performed in duplicate using independent biosensors ($n = 2$). Finally, the peak centroid or center of gravity statistics of ten sensor chips was estimated using OriginPro Software analysis functions, the coefficient of variation CV was considered as the ratio of the standard deviation σ to the mean m according to the following formula: $CV = (\sigma/m) \times 100\%$.

Supporting Information

Supporting Information is available from the Wiley Online Library or from the author.

Conflict of Interest

The authors declare no conflict of interest.

Author Contributions

J.M.F.-C. and M.A.O. contributed equally to this work. J.M.F.-C., M.A.O., and J.R.-A. contributed to conceptualization. J.M.F.-C., M.A.O., J.R.-C., G.L.-M., and J.Y. contributed to methodology. J.M.F.-C., M.A.O., J.R.-C., G.L.-M., J.Y., L.M.-F., M.F.-G., E.M.-L., and A.T.-V. carried out the investigation. J.M.F.-C. contributed to visualization. J.M.F.-C., M.A.O., and J.R.-A. supervised the project. J.M.F.-C., M.A.O., J.R.-C., G.L.-M., J.Y., and J.R.-A. wrote the original draft. J.M.F.-C., M.A.O., J.R.-C., G.L.-M., J.Y., and J.R.-A reviewed and edited the writing.

Data Availability Statement

The data that support the findings of this study are available in the supplementary material of this article.

[1] D. E. Ingber, *Nat. Rev. Genet.* **2022**, *23*, 467.
[2] D. Huang, X. Zhang, X. Fu, Y. Zu, W. Sun, Y. Zhao, *Eng. Regener.* **2021**, *2*, 246.
[3] O. Tatsuya, S. G. M. Uzeland, R. D. Kamm, *Sci. Adv.* **2022**, *4*, eaat5847.
[4] J. H. Sung, C. Kam, M. L. Shuler, *Lab Chip* **2010**, *10*, 446.
[5] Y. Imura, K. Sato, E. Yoshimura, *Anal. Chem.* **2010**, *82*, 9983.
[6] K. Ronaldson-Bouchard, D. Teles, K. Yeager, D. N. Tavakol, Y. Zhao, A. Chramiec, S. Tagore, M. Summers, S. Stylianos, M. Tamargo, B. M. Lee, S. P. Halligan, E. H. Abaci, Z. Guo, J. Jacków, A. Pappalardo, J. Shih, R. K. Soni, S. Sonar, C. German, A. M. Christiano, A. Califano, K. K. Hirschi, C. S. Chen, A. Przekwas, G. Vunjak-Novakovic, *Nat. Biomed. Eng.* **2022**, *6*, 351.
[7] "International Diabetes Federation (IDF), IDF Diabetes Atlas – Tenth edition **2021**," https://diabetesatlas.org/atlas/tenth-edition/.
[8] N. H. Cho, J. E. Shaw, S. Karuranga, Y. Huang, J. D. da Rocha Fernandes, A. W. Ohlrogge, B. Malanda, *Diabetes Res. Clin. Pract.* **2018**, *138*, 271.
[9] M. P. Corcoran, S. Lamon-Fava, R. A. Fielding, *Am. J. Clin. Nutr.* **2007**, *85*, 662.
[10] T. Nedachi, H. Fujita, M. Kanzaki, *Am. J. Physiol. Endocrinol. Metab.* **2008**, *295*, E1191.
[11] B. Hellman, E. Gylfe, E. Grapengiesser, H. Dansk, A. Salehi, *Lakartidningen* **2007**, *104*, 2236.
[12] M. Prentki, C. J. Nolan, *J. Clin. Invest.* **2006**, *116*, 1802.
[13] J. M. Fernández-Costa, X. Fernández-Garibay, F. Velasco-Mallorquí, J. Ramón-Azcón, *J. Tissue Eng.* **2021**, *12*, 204173142098133.
[14] S. A. Langhans, *Front. Pharmacol.* **2018**, *9*, 6.
[15] A. M. Ghaemmaghami, M. J. Hancock, H. Harrington, H. Kaji, A. Khademhosseini, *Drug Discovery Today* **2012**, *17*, 173.
[16] F. Velasco-Mallorquí, J. Rodríguez-Comas, J. Ramón-Azcón, *Biofabrication* **2021**, *13*, 035044.
[17] A. Kang, J. Park, J. Ju, G. S. Jeong, S.-H. Lee, *Biomaterials* **2014**, *35*, 2651.
[18] T. Osaki, V. Sivathanu, R. D. Kamm, *Biomaterials* **2018**, *156*, 65.
[19] A. B. Theberge, J. Yu, E. W. K. Young, W. A. Ricke, W. Bushman, D. J. Beebe, *Anal. Chem.* **2015**, *87*, 3239.
[20] S. G. M. Uzel, R. J. Platt, V. Subramanian, T. M. Pearl, C. J. Rowlands, V. Chan, L. A. Boyer, P. T. C. So, R. D. Kamm, *Sci. Adv.* **2016**, *2*, e1501429.
[21] N. R. Wevers, R. van Vught, K. J. Wilschut, A. Nicolas, C. Chiang, H. L. Lanz, S. J. Trietsch, J. Joore, P. Vulto, *Sci. Rep.* **2016**, *6*, 38856.
[22] S. Oh, H. Ryu, D. Tahk, J. Ko, Y. Chung, H. K. Lee, T. R. Lee, N. L. Jeon, *Lab Chip* **2017**, *17*, 3405.
[23] K.-J. Jang, K.-Y. Suh, *Lab Chip* **2010**, *10*, 36.
[24] H. Suzuki, T. Hirakawa, I. Watanabe, Y. Kikuchi, *Anal. Chim. Acta* **2001**, *431*, 249.

**ADVANCED
SCIENCE NEWS**

www.advancedsciencenews.com

**ADVANCED
MATERIALS
TECHNOLOGIES**

www.advmattechnol.de

[25] L. Wang, M. A. Acosta, J. B. Leach, R. L. Carrier, *Lab Chip* **2013**, *13*, 1586.

[26] D. L. Bellin, H. Sakhtah, J. K. Rosenstein, P. M. Levine, J. Thimot, K. Emmett, L. E. P. Dietrich, K. L. Shepard, *Nat. Commun.* **2014**, *5*, 3256.

[27] S. E. Eklund, D. E. Cliffel, E. Kozlov, A. Prokop, J. Wikswo, F. Baudenbacher, *Anal. Chim. Acta* **2003**, *496*, 93.

[28] M.-H. Wu, J.-L. Lin, J. Wang, Z. Cui, Z. Cui, *Biomed. Microdevices* **2009**, *11*, 265.

[29] Y. Gong, Z. Chen, L. Yang, X. Ai, B. Yan, H. Wang, L. Qiu, Y. Tan, N. Witman, W. Wang, Y. Zhao, W. Fu, *ACS Nano* **2020**, *14*, 8232.

[30] R. Obregón, S. Ahadian, J. Ramón-Azcón, L. Chen, T. Fujita, H. Shiku, M. Chen, T. Matsue, *Biosens. Bioelectron.* **2013**, *50*, 194.

[31] J. Rodríguez-Comas, J. Ramón-Azcón, *In Vitro Models* **2022**, *1*, 41.

[32] A. Hernández-Albors, A. G. Castaño, X. Fernández-Garibay, M. A. Ortega, J. Balaguer, J. Ramón-Azcón, *Biosens. Bioelectron.: X* **2019**, *2*, 100025.

[33] M. A. Ortega, X. Fernández-Garibay, A. G. Castaño, F. De Chiara, A. Hernández-Albors, J. Balaguer-Trias, J. Ramón-Azcón, *Lab Chip* **2019**, *19*, 2568.

[34] C. Kelly, N. H. McClenaghan, P. R. Flatt, *Islets* **2011**, *3*, 41.

[35] M. J. Luther, A. Hauge-Evans, K. L. A. Souza, A. Jörns, S. Lenzen, S. J. Persaud, P. M. Jones, *Biochem. Biophys. Res. Commun.* **2006**, *343*, 99.

[36] T. P. J. Solomon, J. M. Haus, K. R. Kelly, M. Rocco, S. R. Kashyap, J. P. Kirwan, *Diabetes Care* **2010**, *33*, 1561.

[37] K. Karstoft, K. Winding, S. H. Knudsen, J. S. Nielsen, C. Thomsen, B. K. Pedersen, T. P. J. Solomon, *Diabetes Care* **2013**, *36*, 228.

[38] F. Dela, M. E. von Linstow, K. J. Mikines, H. Galbo, *Am. J. Physiol.: Endocrinol. Metab.* **2004**, *287*, E1024.

[39] J. Barlow, T. P. J. Solomon, *Metab., Clin. Exp.* **2019**, *91*, 1.

[40] R. Riahi, S. A. M. Shaegh, M. Ghaderi, Y. S. Zhang, S. R. Shin, J. Aleman, S. Massa, D. Kim, M. R. Dokmeci, A. Khademhosseini, *Sci. Rep.* **2016**, *6*, 24598.

[41] A. Weltin, K. Slotwinski, J. Kieninger, I. Moser, G. Jobst, M. Wego, R. Ehret, G. A. Urban, *Lab Chip* **2014**, *14*, 138.

[42] M. A. Ortega, J. Rodríguez-Comas, O. Yavas, F. Velasco-Mallorquí, J. Balaguer-Trias, V. Parra, A. Novials, J. M. Servitja, R. Quidant, J. Ramón-Azcón, *Biosensors* **2021**, *11*, 138.

[43] H. Altug, S. H. Oh, S. A. Maier, J. Homola, *Nat. Nanotechnol.* **2022**, *17*, 5.

[44] G. A. Lopez, M. C. Estevez, M. Soler, L. M. Lechuga, *Nanophotonics* **2017**, *6*, 123.

[45] N. Picollet-D'hahan, A. Zuchowska, I. Lemeunier, S. le Gac, *Trends Biotechnol.* **2021**, *39*, 788.

[46] X. Fernández-Garibay, M. A. Ortega, E. Cerro-Herreros, J. Comelles, E. Martínez, R. Artero, J. M. Fernández-Costa, J. Ramón-Azcón, *Biofabrication* **2021**, *13*, 035035.

[47] C. T. Rueden, J. Schindelin, M. C. Hiner, B. E. DeZonia, A. E. Walter, E. T. Arena, K. W. Eliceiri, *BMC Bioinformatics* **2017**, *18*, 529.

[48] F. Velasco-Mallorquí, J. M. Fernández-Costa, L. Neves, J. Ramón-Azcón, *Nanoscale Adv.* **2020**, *2*, 2885.

[49] C. Poon, *J. Mech. Behav. Biomed. Mater.* **2022**, *126*, 105024.

[50] G. A. Lopez-Muñoz, J. M. Fernández-Costa, M. A. Ortega, J. Balaguer-Trias, E. Martin-Lasierra, J. Ramón-Azcón, *Nanophotonics* **2021**, *10*, 4477.

[51] A. Oubiña, B. Ballesteros, P. Bou Carrasco, R. Galve, J. Gascón, F. Iglesias, N. Sanvicens, M.-P. Marco, in *Techniques and Instrumentation in Analytical Chemistry*, (Ed: D. Barceló), Elsevier, New York **2000**, pp. 287–339.